



HAL
open science

Ni-doped CeO₂ nanoparticles to promote and restore the performance of Ni/YSZ cathodes for CO₂ electroreduction

Dingkai Chen, Jinming Zhang, Mathias Barreau, Sylwia Turczyniak-Surdacka, Olivier Joubert, Annie Le Gal La Salle, Spyridon Zafeiratos

► To cite this version:

Dingkai Chen, Jinming Zhang, Mathias Barreau, Sylwia Turczyniak-Surdacka, Olivier Joubert, et al.. Ni-doped CeO₂ nanoparticles to promote and restore the performance of Ni/YSZ cathodes for CO₂ electroreduction. *Applied Surface Science*, 2023, 611, pp.155767. 10.1016/j.apsusc.2022.155767 . hal-03924370

HAL Id: hal-03924370

<https://hal.science/hal-03924370>

Submitted on 19 May 2023

HAL is a multi-disciplinary open access archive for the deposit and dissemination of scientific research documents, whether they are published or not. The documents may come from teaching and research institutions in France or abroad, or from public or private research centers.

L'archive ouverte pluridisciplinaire **HAL**, est destinée au dépôt et à la diffusion de documents scientifiques de niveau recherche, publiés ou non, émanant des établissements d'enseignement et de recherche français ou étrangers, des laboratoires publics ou privés.

Ni-doped CeO₂ nanoparticles to promote and restore the performance of Ni/YSZ cathodes for CO₂ electroreduction

Dingkai Chen,¹ Jinming Zhang,¹ Mathias Barreau,¹ Sylwia Turczyniak-Surdacka,^{2,3} Olivier Joubert,⁴ Annie Le Gal La Salle,⁴ and Spyridon Zafeiratos¹

¹*Institut de Chimie et Procédés pour l'Énergie, l'Environnement et la Santé, UMR 7515 CNRS-UdS, 25 Rue Becquerel, 67087 Strasbourg, France*

²*Faculty of Chemistry, Biological and Chemical Research Centre, University of Warsaw, Żwirki i Wigury 101, 02-089 Warsaw, Poland*

³*Faculty of Chemistry, University of Warsaw, Żwirki i Wigury 101, 02-089 Warsaw, Poland*

⁴*Institut des Matériaux Jean Rouxel (IMN), Université de Nantes-CNRS, 2 Rue de La Houssinière, BP 32229, 44322 Nantes Cedex 3, France*

Abstract

Despite the considerable efforts to develop innovative electrode materials, nickel/yttria-stabilized zirconia (Ni/YSZ) electrodes are still employed in nearly all commercial and industrial solid oxide cell units. This is because Ni/YSZ cermets have good electrocatalytic activity in both electrolysis and fuel cell modes, while they are cost-effective as compared to alternative electrodes under development at the lab scale. Infiltration of nanoparticles has immersed as a promising concept to enhance the performance and robustness of conventional Ni/YSZ. Herein, we apply a relatively simple procedure to infiltrate Ni/YSZ electrodes with hexane solution containing prefabricated Ni-doped CeO₂ nanoparticles. Cells with modified Ni/YSZ electrodes show a great improvement in the electrocatalytic activity and stability towards direct CO₂ reduction as compared to unmodified cathodes. Besides, a single infiltration step is sufficient to achieve the optimum cell performance, streamlining the preparation process. More importantly, we show that this strategy can be equally efficient to fully reactivate previously degraded Ni/YSZ electrodes and restore their electrochemical performance at levels even higher than the initial ones. In addition, due to the high viscosity of the hexane solution, Ni-doped CeO₂ nanoparticles access the entire electrode volume all the way close to the YSZ interface, while it penetrates the micro cracks between Ni and YSZ particles. In this way the electrocatalytic reaction zone is recovered, and the degraded Ni/YSZ electrode is reactivated. Physicochemical, microstructural and electrochemical characterization of the cells evinces several effects that contribute to the performance improvement of Ni/YSZ after infiltration, such as the enhanced surface reducibility of Ni and the amelioration of charge transfer processes within the electrode. The simplicity of the proposed infiltration method and the significant promotion in CO₂ electroreduction activity, advocate it as a cost-efficient strategy to improve or regenerate conventional Ni/YSZ electrodes without significantly altering the already well-established fabrication process.

1. Introduction

Nickel yttria-stabilized zirconia composites (Ni/YSZ cermets) are the most commonly used electrode materials for solid oxide cells (SOCs) cathodes and anodes [1,2]. However, a key challenge for the commercialization of SOC with Ni/YSZ electrodes remains their limited long-term stability, especially under high current density operation conditions [3,4]. This is usually related to microstructural modifications of the Ni/YSZ interface, for example Ni coarsening and migration, or even, formation of ZrO₂ nanoparticles on the Ni surface due to the reduction/re-oxidation of YSZ [5–7]. Ni depletion from its interface with YSZ is accounted for the loss of electrochemical active sites, the so-called triple-phase boundary (TPB), which is regarded as one of the most detrimental factors for the cell performance. In addition, it may lead to the loss of the Ni percolation network, decreasing in this way the electrode conductivity. Therefore, improvement of the microstructural stability of traditional Ni/YSZ electrodes is required in order to boost the long-term performance of SOCs.

Currently, the infiltration of electro-catalyst precursor solutions into a conventional Ni/YSZ electrode appears as an efficient approach to improve the performance and durability of SOCs [6,8–11]. In particular, in case of solid oxide electrolysis cells (SOECs) various materials have been infiltrated to the Ni/YSZ electrode including metals, Ce-based oxides, and perovskite-type oxides [11]. Among them, CeO₂-based compounds are recognized as promising additives because they do not react with Ni or YSZ at standard SOEC operating conditions. Besides, they can create a large amount of TPBs/2PBs and abundant oxygen vacancies, while they can also moderate deactivation at high operating temperatures [11–17]. Several studies have suggested that the addition of ceria-based materials over conventional Ni/YSZ electrodes enhances the activity of the cell for hydrogen evolution and electrocatalytic CO₂ reduction reactions [6,9,11,12,15,17–20]. Moreover, 2PBs on doped-ceria electrodes are capable to deliver high power densities even in the absence of metal catalysts and thus TBPs [21,22] Table 1 provides a non-exhaustive list of studies concerning modification of Ni/YSZ electrodes by CeO₂-based compounds. The great majority of these studies use nitrate solutions as ceria precursor, which very often requires several infiltration steps to achieve the desired loading. In order to reduce the number of infiltration cycles some authors proposed the use of dispersant and surfactant additives in the solution, such as glycol, citric acid, urea or Triton X-100 [9,11,16,17,23]. However, since the additives are specifically associated to the composition of the nano-catalysts and the substrate, each surfactant system needs to be re-engineered every time in order to respond to changes of SOC electrodes or nano-catalyst composition, which evidently complicates the infiltration process.

Table 1. Publications on Ni/YSZ electrodes modified by CeO₂-based compounds (* Gd-doped Ceria or Ce_{0.8}Gd_{0.2}O_{2-x}, ** Mo_{0.1}Ce_{0.9}O_{2+δ}, *** Samaria-doped ceria, **** Lanthanum-doped ceria)

Infiltration material	Infiltration method	Number of infiltration steps	Additive loading (mass loading, solution concentration)	Reference
CeO ₂	Cerium(III) nitrate hexahydrate [Ce(NO ₃) ₃ ·6H ₂ O] with urea and a mixture of water and ethanol;	5	3.38 wt%	[24]
CeO ₂	Commercial colloid (CeO ₂) with CeO ₂ particles suspended in acetic acid under vacuum;	2	1.75 wt%	[25]
GDC*	Cerium nitrate (Ce(NO ₃) ₃ ·6H ₂ O), gadolinium nitrate (Gd(NO ₃) ₃ ·6H ₂ O) dissolved in ethanol; Vacuum process;	Several	9.9 mg of CGC20 per cm ²	[18]
GDC	Nitrate solution Ce(NO ₃) ₃ and Gd(NO ₃) ₃ ; Surfactant PEL62; Two-atmosphere reduction (H ₂ /H ₂ O);	9	~145 mg CGC per 1 cm ³ Ni-YSZ backbone (Ni/YSZ electrode + Ni/YSZ support)	[12]
GDC	Gd(NO ₃) ₃ ·6H ₂ O and Ce(NO ₃) ₃ ·6H ₂ O in distilled water; Triton X-100 and citric acid as surfactant and chelating agent;	1	0.1 M, 0.5 M, 1M, 2M	[9,11]
GDC	GDC nitrate solution; Ce(NO ₃) ₃ , Gd(NO ₃) ₃ and Trix-100 surfactant in a vacuum atmosphere;	5	No description	[15]
GDC	GDC (Ge _{0.8} Gd _{0.2} O _{1.9}) precursor solution; Ce-nitrate and Gd-nitrate; Surfactant PE-L62;	Several	125 mg GDC per 1 cm ³ Ni/YSZ backbone (Ni/YSZ electrode + Ni/YSZ support)	[6]
GDC	GDC nitrate solution; Ce(NO ₃) ₃ and Gd(NO ₃) ₃ ; PE-L62 surfactant;	7	120 mg gdc per 1 cm ³ Ni/YSZ structure (Ni/YSZ H ₂ -electrode + Ni/YSZ support)	[19]
GDC	Ce- and Gd-nitrate salts mixed with water and a surfactant (Triton X-100);	1	2 vol-%	[17]
GDC	Gd(NO ₃) ₃ ·6H ₂ O, Ce(NO ₃) ₃ ·6H ₂ O and urea in water/ethanol co-solvent;	n/a	0.35 and 0.015M GDC	[26]
GDC	Cerium and gadolinium nitrate solutions; glycine;	7-8	0.3M	[27,28]
GDC and Rh-GDC	GDC and Rh-GDC powders solved in butanol-mixed xylene solution and a surfactants	n/a	0.26 and 10.4 mg cm ⁻²	[29]
GDC and Ni-GDC	Ni(NO ₃) ₂ ·6H ₂ O, Gd(NO ₃) ₃ ·6H ₂ O, and Ce(NO ₃) ₃ ·6H ₂ O in ethanol solution with Triton-X 100 surfactant under vacuum;	1	1.26 wt % for GDC; 1.29 wt % for Ni-GDC;	[16]
Ni-GDC	Ni(NO ₃) ₂ ·6H ₂ O, Gd(NO ₃) ₃ ·6H ₂ O, Ce(NO ₃) ₃ ·6H ₂ O, and citric acid dissolved in ethanol;	1	4M	[23]
MDC**	Aqueous solution of Ce(NO ₃) ₃ ·6H ₂ O and (NH ₄) ₆ Mo ₇ O ₂₄ with citric acid under vacuum;	5, 7 and 9	294 mg cm ⁻³ after 7 cycles	[20]
SDC***	Ce(NO ₃) ₃ ·6H ₂ O and Sm(NO ₃) ₂ ·6H ₂ O mixed with glycine;	2	4 wt% SDC	[30]
LDC****	Aqueous solutions of Ce(NO ₃) ₃ ·6H ₂ O, La(NO ₃) ₃ ·6H ₂ O	n/a	10 wt.% LDC	[31]

	in dilute aqueous ammonia;			
--	----------------------------	--	--	--

Recently we reported on a simple infiltration strategy [32] to deposit ceria nanoparticles (NPs) synthesized in hexane solution [33] into the pores of pre-fabricated Ni/YSZ cermet electrodes. This approach offers higher control on the infiltration process and allows preselecting the characteristics of the nanoparticles, since their synthesis is done beforehand. In addition, by this approach a homogenous distribution of high ceria loading into the Ni/YSZ electrode volume even after one infiltration step [32] is achieved. Decoration of Ni/YSZ cathodes with Ni-doped ceria NPs had a strong impact on the CO₂/H₂ electrolysis performance and this was attributed to the formation of an ultrathin Ni-Ce³⁺ layer on the electrode surface. Besides, Ni/YSZ cermets decorated with ceria nanoparticles have high tolerance to oxidation by CO₂ [34], which can potentially slow down deactivation.

At high-temperatures, metallic Ni is easily oxidized to NiO by CO₂, which is a major cause of SOEC performance degradation. Therefore, a reducing gas such as H₂ or CO, sometimes also called safety gas, is usually co-fed with CO₂ into the Ni-YSZ cathode. The unique combination of high electrochemical performance and increased oxidation tolerance of Ni/YSZ cathodes decorated by ceria NPs [32,34], motivated us to explore their performance for direct CO₂ electrolysis, which means without the presence of reducing gas (typically H₂ or CO) in the fuel feed. Please note that elimination of reducing gas, not only simplifies the cell design but also considerably decrease the operation cost of the SOC systems [35]. Indeed, evaluation of button cells demonstrates a spectacular improvement of the Ni/YSZ performance after modification with ceria nanoparticles. In addition, experiments on miniature cells show that impregnation of ceria on deactivated Ni/YSZ electrodes can reestablish the cell performance. A single infiltration step is enough to achieve the optimal ceria NPs loading which is an important advantage for practical applications as compared to previous more elaborated methods.

2. Experimental

2.1. Cell fabrication

The cells tested in this work were electrolyte-supported and were purchased from Kerafol GmbH. They consist of a Ni/YSZ cathode electrode (60wt-%Ni/ 40wt-%YSZ, 35 μm thickness), an 8 YSZ electrolyte (8 mol-% Y₂O₃ stabilized ZrO₂, 150 μm thickness). A thin YSZ interdiffusion barrier layer is used to prevent solid state reactions between the YSZ electrolyte and the Ni/YSZ electrode as well as to improve the thermal expansion matching between them. The anode and the footprint (geometric size) of the cells were adapted to the testing conditions. In particular, the cells tested in the conventional *dual-chamber* button-cell test station were square-shaped with size 20x20mm², with La_{0.6}Sr_{0.4}Co_{0.2}Fe_{0.8}O_{3-δ} (LSCF) as the anode electrode. The cells measured in the *single-chamber* test

station attached to the XPS spectrometer, were 1/4 fragments of a 2 cm diameter disk cell with an active area around 0.64 cm² (hereafter referred as *miniature* cells). In case of miniature cells the anode was a porous Pt layer prepared by sintering of platinum paste (Pt ink 5542-DG, ESL) [32]. Cells from the same production batch were used for the comparison of pristine and Ni/YSZ modified electrodes. The Ni_{0.04}Ce_{0.96}O₂ nanoparticles (hereafter abbreviated as NiCeO_x NPs) were prepared from Schiff base metal complexes and dispersed in hexane solution according to a recently developed procedure [33]. The concentration of NiCeO_x NPs in the hexane solution was calculated on the basis of TGA measurements and found 4.4±0.3 mg/ml. The NiCeO_x NPs solution was drop-casted directly on the top of the pre-reduced Ni/YSZ electrodes using a 10 µL micropipette following a procedure described in detail elsewhere [32]. After drop-casting, the cells were let dry at 80 °C for 30 min and then they were calcined in air at 400 °C for 1 hour. For brevity the cells with pristine Ni/YSZ cathode electrodes will be referred as NiYSZ while those modified with NiCeO_x, as NiCe@NiYSZ.

2.2. Electrochemical characterization

2.2.1. Button cell electrochemical tests

i-V polarization curves and EIS measurements were performed over Ni/YSZ//YSZ//LSCF cells with pristine and modified Ni/YSZ cathode electrodes under direct CO₂ electrolysis conditions (without reducing gas) at 700 °C. The fuel composition was 3% CO₂/97% N₂ with a flow of 300 mL/min, for the cathode electrode, while synthetic air was employed at the anode side at the flow rate of 100 mL/min. The electrochemical tests of the button cells with dimensions 2×2cm² were carried out in a commercial Fiaxell measurement station (Open Flanges™). The cells were placed between soft alumina felts and characterized by linear-sweep voltammetry (LSV), staircase potentiostatic curves and electrochemical impedance spectroscopy (EIS) measurements, using a computer controlled potentiostat/galvanostat (VersaSTAT 3, AMETEK Scientific Instruments). Prior to each electrochemical test, the fuel electrode was pre-reduced for 12h in 5%H₂/95%Ar (50 mL/min) at 700 °C. Subsequently, the measurements were carried out by varying the potential between the open circuit potential (O.C.) value and 2.5 V, at a scan rate of 5 mV/s. The potentiostatic curves are corrected for the ohmic drop induced by the electrolyte and the contact resistances according to the formula : $V_{-iR} = V_{A-C} - (R_{ohm} \times i_{set})$, where R_{ohm} is the ohmic resistance obtained from the high frequency intercept in impedance spectra, i_{set} the applied current density and V_{A-C} the voltage measured between anode and cathode electrodes. The cathode of NiCe@NiYSZ cell was modified with 170 mg/cm³ NiCeO_x NPs following the procedure described in section 2.1.

2.2.2. Miniature cells tests in a single-chamber station attached to an XPS spectrometer

Electrochemical characterization of pristine and NiCeO_x-modified Ni/YSZ electrodes was also performed in a custom-built flow-through reaction chamber attached to an XPS described elsewhere [35,36]. The cells were pressed directly on the ceramic heater using stainless steel clamps, while a gold grid was used on both sides as the current collector. The temperature was controlled by a K-type thermocouple mounted on the heater. The gases were introduced via mass flow controllers and the products were monitored via an *online* quadrupole mass spectrometer (QMS). CO₂ electrolysis was carried out in 100% CO₂ atmosphere (without diluting or reducing gas) in few mbar CO₂ pressure (1-10 mbar), at 550 and 700 °C. Prior to the electrochemical tests, the electrode was calcined for 30 min in 1.0 mbar O₂ at 400 °C to remove residual carbon and organic residuals and then underwent reduction in 1.0 mbar H₂ at 550 °C for 30 min. Subsequently, the gas phase switched to CO₂ and the sample was left to equilibrate for about 1 hour at elevated temperature. A computer controlled potentiostat/galvanostat (VersaSTAT 3, AMETEK Scientific Instruments) was used for the electrochemical measurements. The EIS spectra were recorded in the frequency range of 500 KHz to 0.05 Hz in both galvanostatic and potentiostatic mode. After CO₂ tests, the cell was cooled down to room temperature in CO₂, then the reactor was evacuated down to 10⁻⁷ mbar, and the sample was transferred under vacuum into the analysis chamber for XPS characterization. To exclude possible uncertainties due to differences in the bulk cell characteristics, the electrochemical experiments were performed using the same cell before and after modification with NiCeO_x NPs. For the degradation tests, a simple protocol was developed in order to accelerate the procedure. This protocol consists of repeated reduction/oxidation (redox) treatments in 1.0 mbar H₂ at 650 °C followed by 5.0 mbar O₂ at 400 °C (30 min each). In total 5 redox cycles were applied for the accelerated degradation experiments.

The particular advantage of miniature cells is that after gas treatments and electrochemical tests the sample can be transferred under vacuum for XPS analysis. This can help to identify possible surface impurities or carbon deposition which could affect the electrochemical performance and mask the effect of surface modification. In addition, the single-chamber test station offers the possibility to mount and dismount the cell without danger of destruction/damage, which is much more complicated in conventional button cell test rings. This allows doing electrochemical tests over the same miniature cell before and after impregnation, excluding uncertainties caused by eventual problems in cells reproducibility or differences on cell mounting. In addition, the small geometric size of the miniature cells simplifies the infiltration procedure performed by a micropipette. However, owing to the special cell configuration and conditions adopted for CO₂ electrolysis (low temperature and pressure, low fuel flow, etc.) the electrochemical performance measured in this setup is inferior to that measured in the

conventional button cell tests. Therefore, in this work the performance of pristine and modified Ni/YSZ cathodes is evaluated in comparative basis under identical reaction conditions.

2.3. Materials Characterization

X-ray diffraction patterns were measured with a Bruker D8 advance diffractometer using Cu K α radiation. Raman spectra were acquired using a micro-Raman spectrometer (Horiba LabRam), with excitation wavelength of 532 nm. A 100 \times objective was used to focus the excitation laser to an approximately 1 μ m spot with a laser power of less than 1 mW to avoid heating and damage of the sample. SEM-EDX characterization was carried out with a ZEISS Crossbeam 540X scanning electron microscope with X-FEG cathode. Samples were mounted on aluminum pin stubs with the use of silver cement (Agar Scientific). A focused ion beam (FIB) was applied for cross-sectional sample preparation with an accelerating FIB voltage of 30 keV and a beam current of 100 nA, whereas polishing was performed with 30 keV and 1.5 nA. In order to protect the surface, platinum layer was deposited by ion beam deposition (30 keV, 300 pA). The EDX maps were collected with the X-MAX^N spectrometer (Oxford Instrument) at 15 keV after tilt correction.

Quasi *in situ* X-ray photoelectron spectroscopy (XPS) measurements were performed in a custom-build experimental setup composed by three stainless steel chambers separated by gate valves. The first chamber (base pressure of 2×10^{-9} mbar) is equipped with x, y, z, ϕ sample manipulator with a receiving station for the sample holder, a VSW Class WA hemispherical electron analyzer (150 mm radius) and a monochromatic Al K α X-ray source (1486.6 eV) for XPS measurements. The second chamber (base pressure 5×10^{-7} mbar) is a flow-through reactor (total volume 0.6 liters) equipped with a sample receiving station, a differentially pumped quadrupole mass spectrometer, a gas manifold at the inlet and a motorized gas control valve at the outlet (EVR 116, Pfeiffer) connected with a dry scroll pump. The two chambers are connected via a load-lock chamber allowing fast insertion of the samples into the system. Samples were mounted on a disc-shaped holder design by OmniVac. The holder is equipped with a pyrolytic boron nitride (PBN) heater, a K-type thermocouple attached on the side of the heater and 3 available electrical contacts used to perform electrochemical measurements. The holder is transferred between the 3 chambers by the use of 3 transfer arms. After pretreatment or electrochemical reaction, the sample was first cooled to room temperature in gas, then the reactor was evacuated down to 10^{-7} mbar, and then the sample was transferred under vacuum into the UHV chamber for XPS characterization. Survey and high-resolution XPS spectra were collected using pass energies of 90 and 44 eV respectively. The nominal FWHM of Ag 3d peak measured on a standard polycrystalline silver foil with 44 eV pass energy was 0.85 eV which is a measure of the instrument resolution. The number of scans in the high resolution spectra were adjusted so as the signal to noise ratio to be higher than 16. During XPS measurements the sample temperature was kept around 230 $^{\circ}$ C

to enhance sample conductivity and prevent electrostatic charging problems. This was confirmed by the binding energy (BE) of the C1s peak at 284.6 eV or in the absence of C 1s signal via the u''' peak of Ce 3d spectrum at 917.1 eV. The peak fitting of Ni 2p and Ce 3d peaks was performed by using peak profiles recorded on reference samples following a method developed earlier [37,38] and described in detail in the supporting information.

3. Results and discussion

3.1. CO₂ electrolysis over pristine and NiCeO_x-modified Ni/YSZ cells tested in a conventional dual-chamber button cell setup

3.1.1 i-V polarization curves

The CO₂ electrolysis performance of pristine (NiYSZ) and NiCeO_x-modified (NiCe@NiYSZ) Ni/YSZ electrodes originating from the same synthesis batch, was at first evaluated by LSV at 700 °C in 3% CO₂/97% N₂. The fuel electrodes were initially reduced in H₂ and then the gas switched to CO₂ and left to equilibrate for about 5 min. During this period the open circuit voltage (O.C.) of the two electrodes gradually decreased due to NiO formation [35]. Just before polarization the O.C. for NiYSZ and NiCe@NiYSZ cells was -200 mV and -733 mV respectively. For comparison, the O.C. measured in CO₂/H₂ fuel (50/50) was found -890 (NiYSZ) and -960 mV (NiCe@NiYSZ). The systematically lower O.C. values of NiCe@NiYSZ are in accordance with the resistance of NiCe@NiYSZ to oxidation by CO₂ [34].

Figure 1a compares the evolution of the current density of the two cells while the potential is swept linearly between anode and cathode (sweep rate 5 mV/s). Notably, the current density of NiCe@NiYSZ cell is considerably higher than that of NiYSZ. For example, at an applied voltage of 1.5 V the current density of NiCe@NiYSZ cell is 135 mA cm⁻², approximately 3 times higher than that of the NiYSZ cell (43 mA cm⁻²). This is a clear indication that infiltration of NiYSZ electrodes with NiCeO_x nanoparticles remarkably enhances the electrocatalytic activity for direct CO₂ electrolysis. A similar tendency is also confirmed by the staircase potentiostatic tests, where the current is measured after 5 min stabilization at each applied potential. The evolution of the cell current density when stepping up the cell voltage, this time corrected for the iR drop, is shown in the inset of Figure 1. The i-V curves for both samples are approximately linear, with the NiCe@NiYSZ electrode operating at significantly lower voltages (for example at 120 mA the difference of the two electrodes is 330 mV).

Characteristic Nyquist plots of the EIS spectra recorded at 1.45 V are displayed in Figure 1b, while the Ohmic (R_{ohm}) and polarization (R_p) resistances at various applied voltages based on EIS spectra, are shown in Figure 1c. We recall here that in the Nyquist plot the R_{ohm} corresponds to the high frequency intercept on the real-axis, whereas the R_p is the distance between the highest and the lowest

frequency intercepts. The R_{ohm} mainly originates from the resistance of ionic transportation inside the electrolyte; however the contribution of the electrode conductance should be also taken into account, especially in case of oxidative fuels like CO_2 . The R_p is related to the reaction kinetics of the electrocatalytic CO_2 reduction. Phenomena such as diffusion and conversion of CO_2 and charge transfer appear at different frequencies, which can be potentially discriminated in EIS spectra. However, since these frequencies highly overlap, a complex analysis is necessary to gain meaningful information from EIS spectra [39]. This requires systematic variations of the operating parameters (temperature, current, gas composition, etc.) so as to identify which processes are affected. Therefore, a detailed analysis of the EIS spectra was not carried out in the present study and the Nyquist plots were mainly used to determine R_{ohm} and R_p and assess the relative performance of the materials.

However, two semicircles at high and low frequencies are clearly distinguished in the Nyquist plots (Figure 1b, and S1), which allows a qualitative comparison of the two samples. In general, the high-frequency arc (R1) is related to charge transfer, while the one at low-frequency (R2) corresponds to mass transfer and gas diffusion processes [40,41]. The Nyquist plots (Figure S1) show a remarkable decrease of R1 in case of NiCe@Ni/YSZ as compared to Ni/YSZ for all applied voltages. This signifies that NiCeO_x NPs improve the charge transfer and accordingly reduce the high-frequency polarization resistance. In contrast, the R2 for NiCe@Ni/YSZ cell is not obviously reduced, meaning that the decrease in the total polarization of modified Ni/YSZ is dominated by charge transfer (related to R1). The acceleration of charge transfer processes has therefore a major contribution to the enhanced electrochemical performance. Overall, the substantial decrease of both R_{ohm} and R_p values at all applied potentials after NiCeO_x infiltration (Figure 1c), denotes that the performance improvement is related to the amelioration of both conductivity and reaction kinetics of the electrode.

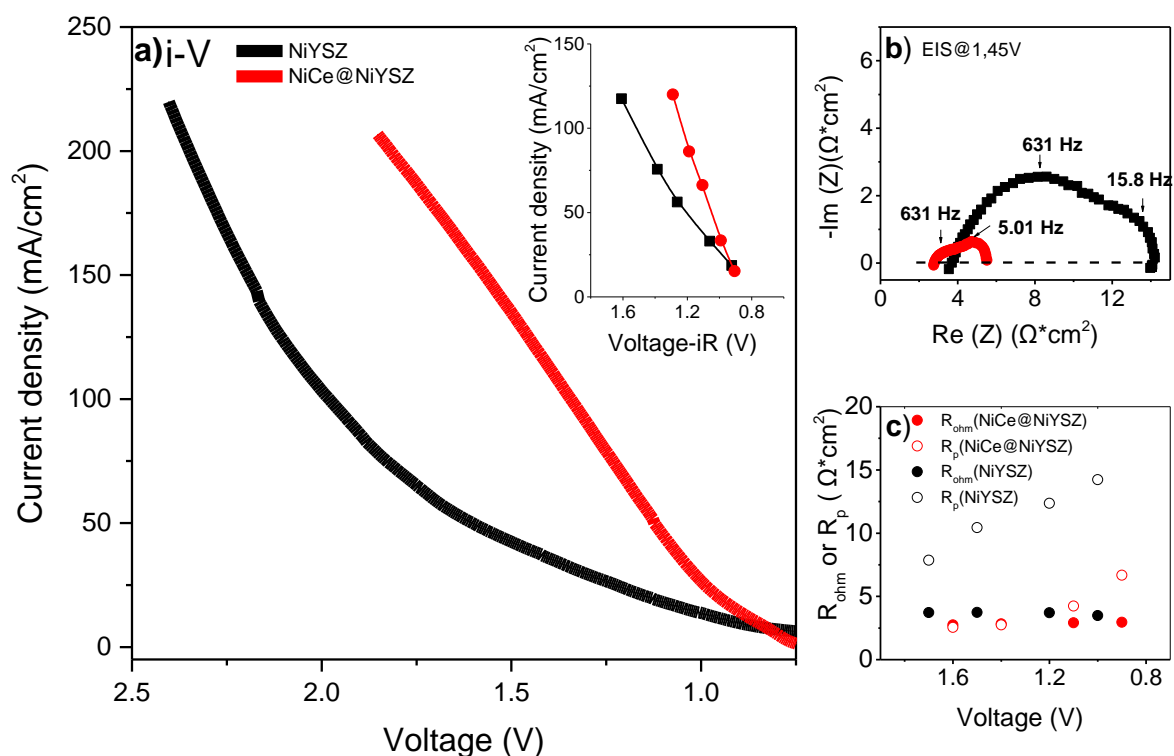


Figure 1. Comparison of CO₂ electrolysis performance between cells with NiYSZ (black) and NiCe@NiYSZ (red) cathode electrodes, **a)** Linear-sweep polarization (scan rate: 5 mV s⁻¹) and (inset) staircase potentiostatic i-V curves, **b)** Nyquist plots of NiYSZ (black) and NiCe@NiYSZ (red) recorded at 1.45 V potentiostatic conditions, **c)** the ohmic (R_{ohm}) and polarization (R_p) resistances determined from the impedance data as a function of the applied voltage. All experiments were carried out at 700 °C in a conventional dual-chamber test station at 1 bar. Cathode-side inlet flow: 3% CO₂/97% N₂ (300 mL/min), anode-side inlet flow: synthetic air (100 mL/min).

3.1.2 Post-mortem spectroscopic and microscopic characterization of the cells

FIB/SEM combined with EDX mapping was employed to analyze the microstructure inside the NiYSZ and NiCe@NiYSZ electrodes after 4h CO₂ electrolysis at 700 °C. In the cross-sectional SEM-EDX mapping shown in Figure 2, the Ni and Zr (from YSZ) phases can be clearly distinguished (blue and green areas respectively). As expected, Ce (red) is detected in case of the NiCe@NiYSZ electrode (figure 2b). Owing to the low NiCeO_x loading, the Ce signal is also relatively low, however it is evenly distributed into the Ni/YSZ electrode volume, including also the parts close to the interface with the YSZ barrier layer. This observation confirms the homogenous distribution of NiCeO_x achieved by the applied method and signifies that this uniformity is preserved during CO₂ electrolysis. In the high-magnification SEM/EDX image of NiYSZ shown in figure 2a and figure S2a, some areas where Ni and YSZ phases are detached can be seen close to the interface with the YSZ electrolyte. These effects have been previously connected with loss of TPB area and performance degradation. In case of

NiCe@NiYSZ, high-magnification images show that apart from areas with high ceria concentration (clearly distinguished in the low-magnification), ceria at lower concentration can be found around Ni and YSZ areas (see also figure S2b). Interestingly NiCeO_x have penetrated narrow electrode channels (i.e. pores) potentially preventing loss of the TPB area found in the NiYSZ electrode.

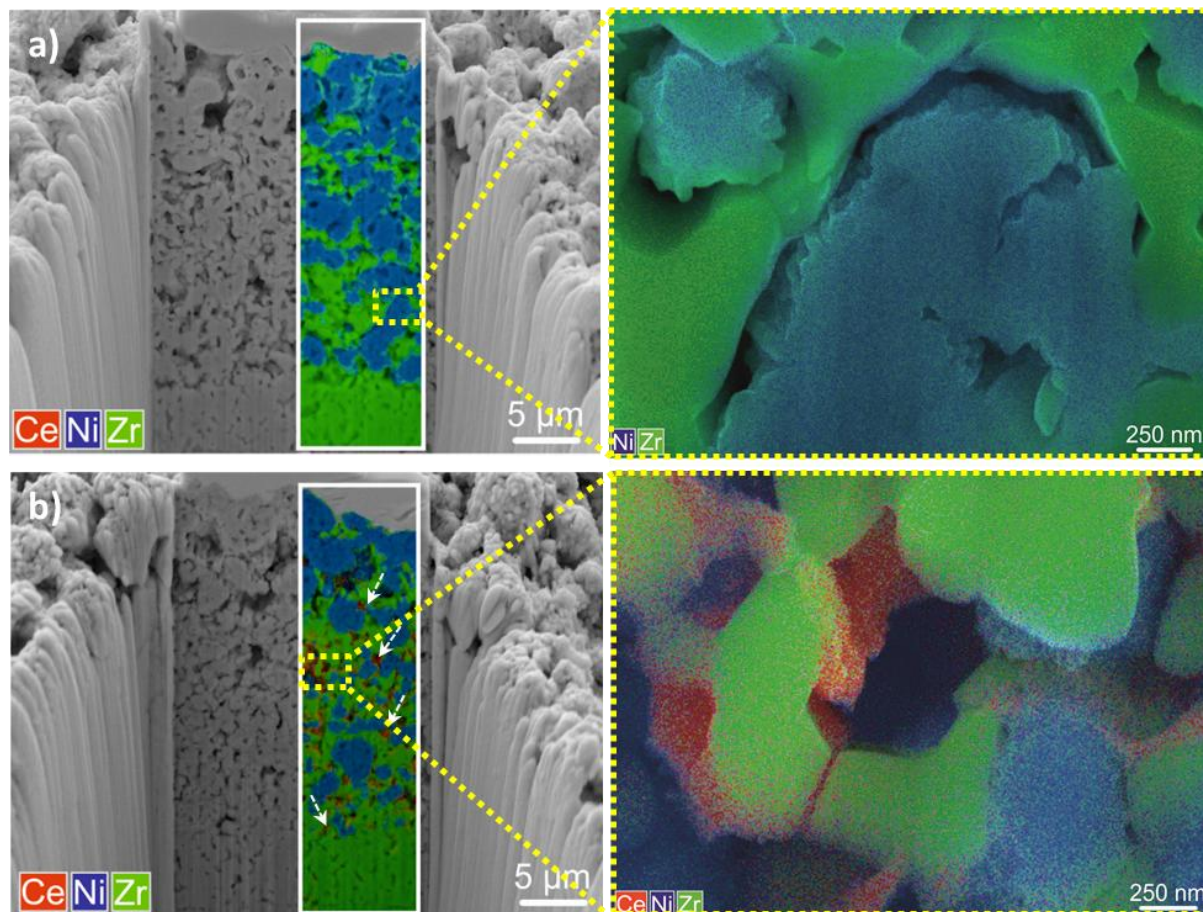


Figure 2. Cross-sectional FIB/SEM images with EDX-mapping of **a)** NiYSZ and **b)** NiCe@NiYSZ cathodes measured after several hours of CO₂ electrolysis. High-magnification images of selected electrode areas are included.

The FIB/SEM images demonstrate the uniform distribution of NiCeO_x NPs into the Ni/YSZ electrode volume and the ability of the NPs to penetrate into narrow electrode channels. These morphological characteristics are compatible with EIS spectra of Figures 1b and S1. In particular, the enhancement of charge transfer processes during CO₂ electrolysis, manifested by the decrease of the high-frequency arc in the EIS spectra, can be explained by the creation of additional CO₂ electrolysis sites related to NiCeO_x NPs deposited over Ni and YSZ grains. Indeed, introduction of NiCeO_x contribute to the electrochemical active area due to the formation of two-phase boundaries between ceria and the gas phase [22,32]. Since the electrode area close to the interface with YSZ electrolyte has a major contribution to the electrochemical reaction [42], penetration of NiCeO_x deep inside the electrode volume, manifested by FIB/SEM, further supports this scenario. In addition to the enhancement of charge transfer processes, EIS results showed a clear improvement in the electrode conductivity

manifested by the decrease in R_{ohm} . This can be due to $NiCeO_x$ NPs inserted in the narrow channels between Ni and YSZ grains (figure 2b). As will be discussed below based on XPS results, the enhanced nickel reducibility after $NiCeO_x$ impregnation is an additional factor promoting electrode conductivity.

Figure 3 shows the Raman spectra and the XRD patterns for NiYSZ and NiCe@NiYSZ cathodes measured after CO_2 electrolysis tests. As expected, the XRD patterns (Figure 3a) are dominated by the diffraction peaks of Ni, NiO and YSZ of the NiYSZ cermet. In case of NiCe@NiYSZ, additional XRD peaks characteristic of cerium oxide were found. According to the Debye-Scherrer equation, the calculated crystalline size of $NiCeO_x$ particles was estimated near 13.2 ± 0.2 nm. This result shows that the nanosized ceria particles, initially infiltrated inside the electrode preserve their dimensions during electrolysis reaction at 700 °C. Besides, it is worth noting that despite the reducing pretreatment in H_2 , NiO peaks are observed in the XRD for both electrodes. This indicates that Ni phase were oxidized either during transfer from the test station to the XRD diffractometer or in the course of CO_2 electrolysis experiment.

Figure 3b presents the Raman spectra of the two electrodes after electrolysis. The Raman peak of unmodified NiYSZ at ca. 620 cm^{-1} is ascribed to the E_g vibration mode of zirconia [43,44]. In case of NiCe@NiYSZ, apart from the E_g band of Zr, an additional peak appears around 460 cm^{-1} due to the F_{2g} peak of cerium oxide [45]. The peak shape found after subtraction of the 2 spectra does not show significant contribution of defect sites typically found around 550 cm^{-1} . Besides, peaks at 1340 and 1570 cm^{-1} ascribed to D (amorphous carbon) and G (graphite) bands [43,44] were not observed in any of the electrodes (see inset of Figure 3b), indicating low or not at all carbon deposition during CO_2 electrolysis.

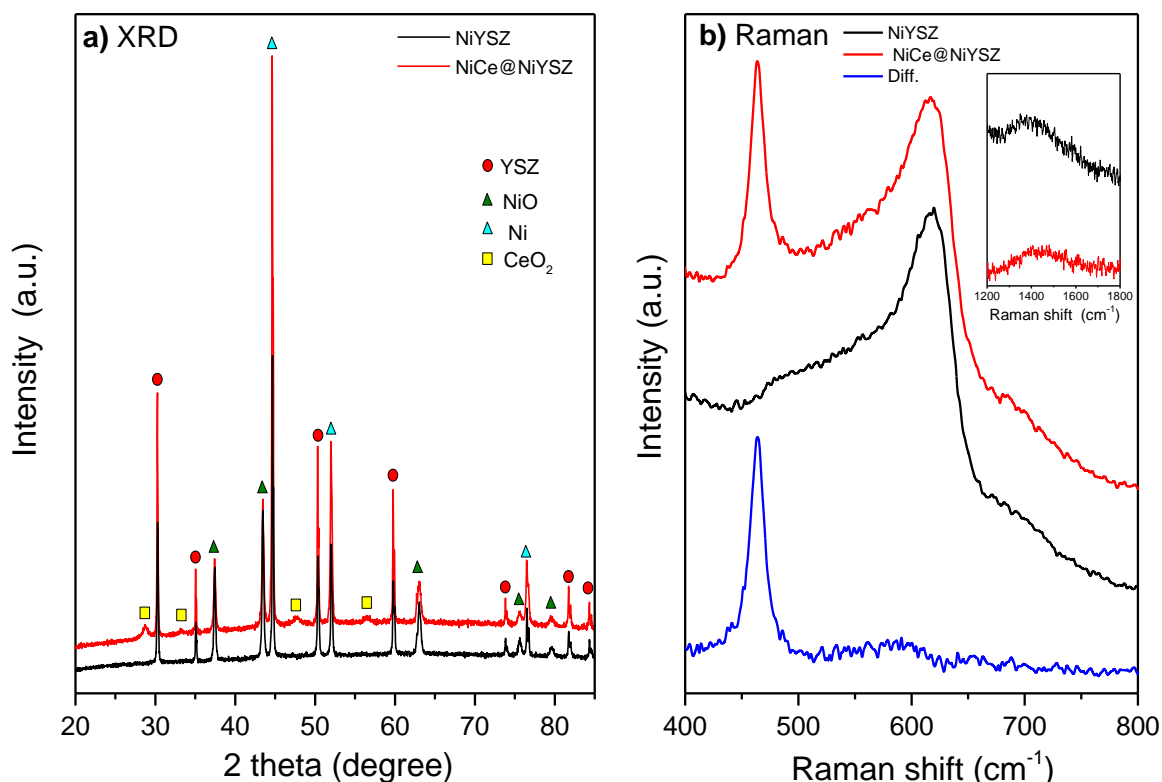


Figure 3. a) XRD patterns and b) Raman spectra of NiYSZ and NiCe@NiYSZ electrodes after several hours CO₂ electrolysis tests at 700 °C. The inset shows the frequency range which corresponds to Raman peaks of carbon species.

3.2. CO₂ electrolysis over pristine and NiCeO_x-modified miniature Ni/YSZ electrodes tested in a single-chamber electrochemical cell

3.2.1 Optimization of NiCeO_x NPs loading over modified NiYSZ cathodes

Next, we determine the optimal NiCeO_x NPs loading for the CO₂ electrochemical performance of NiYSZ cells. To do so, a single-chamber setup was used, permitting facile mounting and dismounting of the cells (no use of glass sealant). This setup allows evaluating the electrocatalytic performance of the same miniature NiYSZ electrode (effective area 64 mm²) before and after infiltration with progressively increasing NiCeO_x NPs loading. Figure 4a displays CO₂ electrolysis i-V curves (corrected for the iR drop) at 700 °C for the NiYSZ electrode before and after modification with 85, 170, and 340 mg/cm³ NiCeO_x NPs. At first, it is verified that the operation of the miniature cells tested in the single-chamber is qualitatively similar with the results observed in the conventional two chamber setup presented above. As shown in Figure 4a, the current densities are about 2 to 3 times lower from those of the conventional testing rig shown in Figure 1a, which can be explained by the differences in the cell mounting and CO₂ pressure. However, the trend in the i-V curves between pristine and modified NiYSZ electrodes is reproduced with the latter cell generating systematic higher current densities. This

validates the use of the results obtained in the single-chamber setup for comparing the electrochemical performance of different electrodes. With this in mind, we compare in Figure 4a the current density between pristine and infiltrated NiYSZ as a function of the cell voltage. Apparently, at certain potentials the NiCeO_x-modified cells produce up to 8 times higher current density as compared to NiYSZ, which is much higher than the values observed in the conventional test rig. Interestingly the most significant improvement in the current is found for the initial infiltration with 85 mg/cm³ NiCeO_x, while higher loadings either have little effect (170 mg/cm³) or even decrease the cell current (340 mg/cm³).

The EIS results at each applied voltage are shown in Figure S3 in the form of Nyquist plots, while the corresponding R_{ohm} and R_p resistances are inserted in Figure 4b. The combination of low CO₂ pressure (1 mbar) and relatively high cell currents induces diffusion limitation problems, since the concentration of CO₂ electroactive species at the electrode surface is finite. Such phenomena are clearly manifested in the low frequency range of Nyquist plots (Figure S3) and complicate the estimation of R_p, especially at high current densities. This is the reason why the inset of Figure 4b contains R_p values only at low applied voltages (i.e. low cell currents). Nevertheless, a decrease in both ohmic and polarization resistances is evident upon infiltration, similar to the observation in the dual-chamber tests (Figure 1c). Note that the lower R_{ohm} is observed in case of the 85 mg/cm³ NiCe@NiYSZ, while at higher loadings it increases and becomes even higher than that of NiYSZ for 340 mg/cm³ NiCe@NiYSZ. This increase might be the effect of oxidative and reducing (redox) treatments following up each infiltration step, as will be discussed below.

To evaluate the effect of the redox treatment on the electrochemical performance, we carried out a “placebo” experiment, where NiYSZ electrodes are infiltrated with hexane solvent (not containing NiCeO_x NPs) and subsequently subjected to a calcination/reduction cycle. As shown in Figure S4 hexane infiltration and the consequent redox cycles deactivate the electrode (at 1.8 V the current density drops at about 40% of its initial value after 4 infiltration and redox cycles). This experiment not only identifies NiCeO_x NPs as the cause of Ni/YSZ electrochemical performance but also indicates the necessity to minimize the number of redox treatments in order to preserve the electrode performance stability.

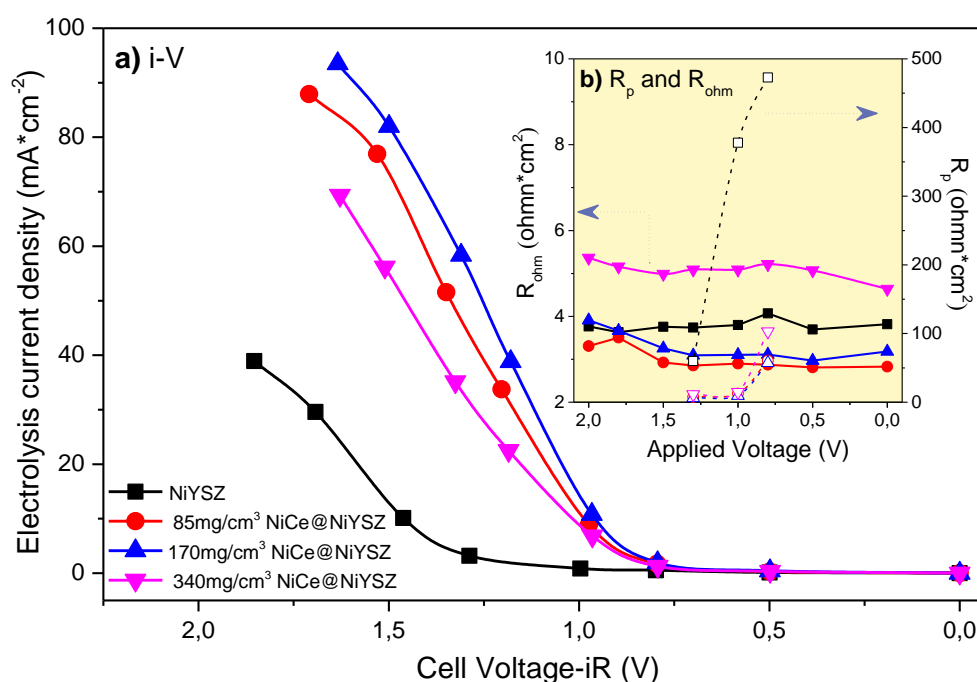


Figure 4. a) i-V curves measured over NiYSZ electrode before and after infiltration with 85, 170, and 340 mg/cm³ NiCeO_x NPs, **b)** the ohmic (R_{ohm}) and polarization (R_p) resistances determined from the impedance data as a function of the applied voltage. All experiments were carried out at 700 °C in a single-chamber test station at 1 mbar CO₂. Please note that different loadings were impregnated consequently on the same NiYSZ electrode.

Taking into account that the improvement in case of 170 mg/cm³ loading is marginal as compared to the 85 mg/cm³ one, it is suggested that the optimal loading is 85 mg NiCeO_x NPs per cm³ of NiYSZ electrode. This result is extremely interesting for practical applications, since this loading can be achieved in a single infiltration/co-firing step. The decrease in the performance observed at very high loadings can be attributed to two possible reasons. The first is that ceria NPs aggregate and accumulate into the electrode pores, limiting gas diffusion, also leading to the increase of the R_p observed for 340 mg/cm³ NiCe@NiYSZ. Another reason is the higher ohmic resistance of the electrode. The considerable increase of R_{ohm} for 340 mg/cm³ found in the EIS spectra suggests that the electrode conductivity, and not the kinetics of the reaction, is the main limiting factor that defined the highest NiCeO_x loadings.

3.2.2 Gas phase and quasi in situ XPS surface analysis of pristine and modified NiYSZ electrodes operating at 550 °C

The single-chamber cell allows monitoring the electrodes by XPS before and after the electrochemical tests without exposure in air (referred here as *quasi in situ* analysis). The aim is to detect eventual differences in the chemical state and composition of pristine and modified NiYSZ. These experiments

were performed at lower temperature (550 °C) in order to slow down the transformation kinetics of the electrode and facilitate their detection by XPS [46]. In addition, higher CO₂ pressure was used (10 instead of 1 mbar) in order to enhance the oxidation effect of CO₂ on nickel [35] similar to the atmospheric CO₂ pressure experimental conditions. The potentiostatic i-V curves and the EIS measurements of NiYSZ and NiCe@NiYSZ cells recorded at 550 °C in ca. 10 mbar CO₂ are shown in Figure S5. The experiments before and after infiltration were carried out at the same NiYSZ cell. As expected, the cell current at 550 °C is inferior to that measured at 700 °C, however the improvement in the performance after infiltration is well reproduced. The Nyquist plots recorded at 1.5 V (Figure S5b), show a decrease of R_p and R_{ohm} for NiCe@NiYSZ, in qualitative agreement with the measurements in the button cell setup. Finally, *online* gas phase analysis demonstrates considerably higher CO and O₂ production in case of the modified electrodes (Figure S5c), confirming that the higher currents are due to the enhanced CO₂ electroreduction rates.

Having shown that the two cells tested in the single-chamber follow qualitatively similar CO₂ electroreduction performance with that of the conventional test rig, we analyze now the surface state of the cathode electrode by XPS. The Ni 2p and Ce 3d (in case of modified electrode) XPS spectra recorded on pristine and modified NiYSZ after CO₂ electrolysis are presented in Figure 5. The two cells were tested at galvanostatic mode, applying the same current to assure operation at identical CO₂ electroreduction rates. Please note that in case of the NiCe@NiYSZ electrode, the Ni 2p and Ce 3d peaks partly overlap (Figure 5b). As shown previously, despite the H₂ pretreatment, Ni is oxidized to NiO at CO₂ pressure above 5 mbar [34,35], which is confirmed by the Ni 2p spectra measured at O.C. (bottom of Figure 5). In particular, the Ni 2p_{3/2} peak is centered at 855.8 eV and is accompanied by a satellite peak shifted by 6.2 eV at higher binding energies, characterizing NiO formation [47]. After CO₂ electrolysis, the new feature at the lower binding energy side of the Ni 2p spectrum, indicates partial reduction of NiO to Ni. The reduction of NiO is enhanced with the current density for both electrodes. A similar behavior was previously observed for Ni-GDC electrodes and was attributed to NiO decomposition upon polarization [35].

The deconvolution of the Ni 2p peak into Ni and NiO compounds using peak profiles of reference samples described in the supporting information, suggests that metallic Ni is systematically higher for NiCe@NiYSZ. For example, at 1.3 mA·cm⁻² 51% of NiO is reduced to Ni for NiCe@NiYSZ, instead of 38% in case of NiYSZ. Please note that according to our previous study, CO₂ electrolysis primarily takes place at the TPB of metallic Ni and reduced ceria [35]. Therefore, the higher amount of metallic Ni at the surface of the electrode is expected to play a key role to the enhanced CO₂ electrolysis performance of the NiCe modified Ni/YSZ electrode. The Ce3d spectrum (Figure 5b) has three pairs of spin-orbit doublets and an intense peak around 917 eV, which is characteristic of the Ce⁴⁺ oxidation

state [48]. The fitting procedure using Ce3d peak profiles of reference Ce^{3+} and Ce^{4+} , reveals that NiCeO_x NPs are in a mixed 55% Ce^{3+} /45% Ce^{4+} oxidation state, which remains practically unaffected by the magnitude of the applied current. The detection of Ce^{3+} cations is intriguing taking into account that direct CO_2 electrolysis takes place under highly oxidative conditions. Notably, these species are accompanied by oxygen vacancies in ceria lattice and have been previously correlated with the increase of conductivity and surface activity of ceria [49]. Therefore, it is feasible that they contribute to the electrochemical reaction, by extending the electrochemically active surface area.

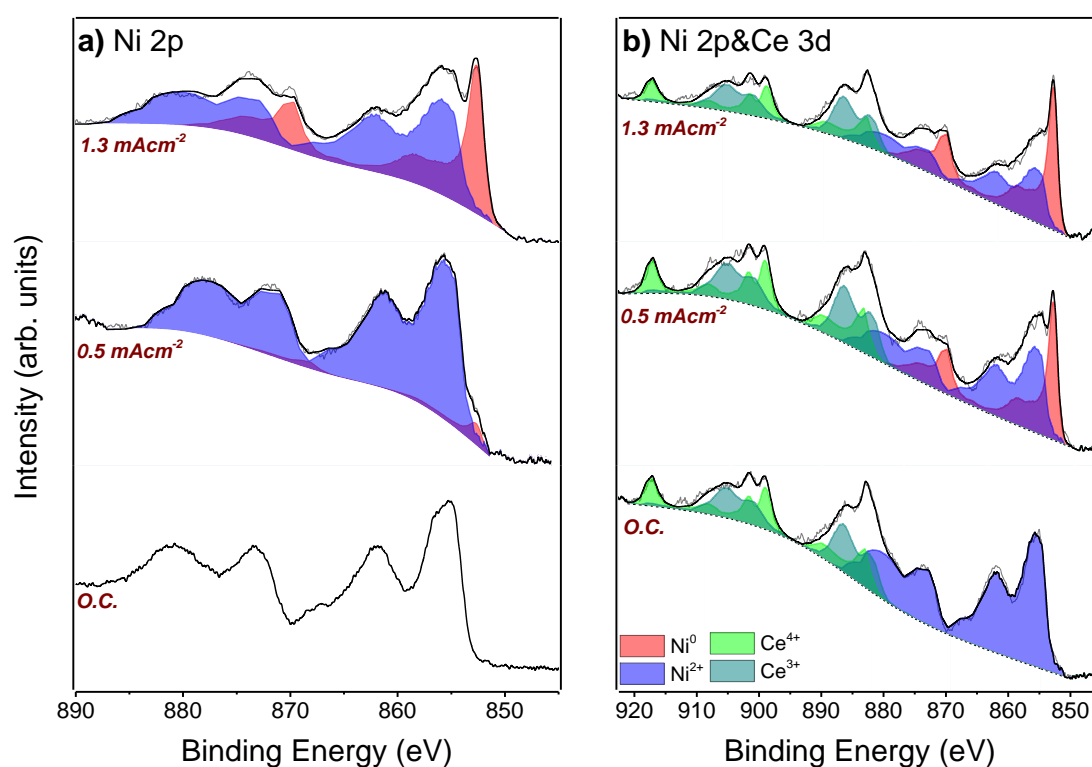


Figure 5. a) Quasi in situ Ni 2p XPS spectra of NiYSZ electrode and b) Ni 2p and Ce 3d XPS spectra of NiCe@NiYSZ electrode. In both cases the spectra were recorded after operation at 550 °C in ca. 10 mbar CO_2 at O.C., 0.5 and 1.3 $\text{mA}\cdot\text{cm}^{-2}$. Prior to CO_2 exposure, both electrodes were reduced in H_2 .

3.2.3. Reactivation of aged Ni/YSZ cathodes by infiltration with NiCeO_x NPs

Modification of the Ni/YSZ electrode microstructure can be induced upon reduction and oxidation (redox) cycles, for example after shutdown. The redox cycles can accelerate the degradation of the cell, typically due to the loss of TPBs [17,50]. In particular, in oxidative conditions, the volume expansion of nickel oxide phase, and the consequent shrinkage induced in the following reduction step, will lead to mechanical stress and eventually to microstructural changes such as crack formation or detach between Ni and YSZ phases. These effects are irreversible and result in a permanent cell failure. In this section we examine the possibility to reactivate degraded NiYSZ electrodes, by post-

mortem infiltration with NiCeO_x NPs. Since in a conventional button cell setup it is extremely complicated to access and modify the surface of the electrode after testing, these tests were performed in the single-chamber setup. In order to accelerate the degradation of the pristine NiYSZ electrode, the cell was subjected in several redox cycles in H₂ and O₂ atmospheres (see also section 3.2.1). Each redox treatment was followed by direct CO₂ electrolysis tests in 1 mbar CO₂ at 550°C for 60 min under a constant applied voltage of -2.0 V. Figure S6 shows the quasi in situ Ni 2p and Ce 3d XPS spectra obtained from the parent and NiCeO_x-modified electrodes after reduction in H₂ and oxidation in O₂. These spectra verify that at the employed conditions nickel and ceria reduce in H₂ and oxidizes in O₂ for both electrodes.

Figure 6a presents the current density and the CO production (bottom) as well as the Ohmic resistance (top) and of the two cells before and after the aging treatment. In case of NiYSZ, the current density drops at about 35 % of its initial value after the 5 redox treatments (for 2.5 hours in total) and 5 hours CO₂ electrolysis tests. As expected, the lower cell currents are followed by lower CO₂ electroreduction rates indicated by the drop of the CO gas phase signal included in Figure 6a. After infiltration of the aged NiYSZ electrode with NiCeO_x NPs the performance not simply improves, but the current density and the CO signal increase by a factor of 3 as compared to those measured initially. When a similar redox aging treatment is applied to the NiCe@NiYSZ (on the same, regenerated cell) causes a drop of the cell current to the 65 % of the initial value. This is significantly less than the drop observed initially on the unmodified NiYSZ (35%). Since pristine and modified Ni/YSZ electrodes were subjected to the same redox protocol, it is reasonable to assume that the observed degradation under redox cycles follows the same mechanism in the two cases, namely detachment between Ni and YSZ phases and eventually microcrack formation. This scenario is supported by the post mortem SEM/EDX analysis of NiCe@NiYSZ electrode (Figure 6b and S7) and the observed increase of R_{ohm} in the EIS spectra (Figure 6a). However, since the introduction of NiCeO_x particles expands the electrochemical active sites from the Ni-YSZ TPB to Ni-NiCeO_x and YSZ-NiCeO_x 2PB the degradation of NiCe@NiYSZ electrode is less important than the one observed on pristine NiYSZ.

The changes in the R_{ohm} resistance measured by the EIS spectra mainly reflects differences in the electrode conductivity, since the electrolyte and temperature remain the same [51]. As shown at the top in Figure 6a, the resistance associated with the charge-transfer reaction (R_{ohm}) particularly increased after the aging treatment in both cases, which is the expected impact of the repeated redox cycles. However, after infiltration of the aged NiYSZ electrode the significant drop in the R_{ohm} resistance indicates an improvement in the conductivity of the electrode. This suggests the creation of new conduction pathways for both electrons and ions, similar to the effects observed for the

infiltration of pristine NiYSZ electrodes. The R_p values could not be determined from the Nyquist plots due to diffusion limitation phenomena similar to figure S3.

We propose two hypotheses to explain the improvement of R_{ohm} of NiYSZ electrode in the presence of NiCeO_x particles. The first is related to the enhanced oxidation tolerance that keeps nickel phase in a partially reduced state, as suggested by the XPS results of figure 5. A second scenario is that the nanoparticles fill in the gap between the cermet phases (Ni and YSZ) promoting in this way the electrode conductivity. This is particularly important to restore the performance of aged electrodes. To examine the second mechanism we perform post mortem microscopy measurements of the aged NiCe@NiYSZ electrode. The cross section SEM/EDX images presented in figure 6b and figure S7 show that NiCeO_x NPs penetrate into the whole volume of the electrode up to the interface with the YSZ electrolyte, also including boundary areas between the Ni and YSZ phases in the cement. This proves that the employed infiltration method is equally efficient for both fresh and aged electrodes. The high magnification SEM/EDX images clearly show the presence of ceria nanoparticles inside nanopore channels (see also figure S7). Consequently it can be argued that infiltrated NiCeO_x nanoparticles may fill in the cracks between Ni and YSZ phases previously formed during the aging redox treatment, and in this way, they repair the microstructure of the deactivated electrode. This has a direct effect in increasing electron and ion percolation pathways between nickel and YSZ phases. A similar mechanism has been previously proposed for GDC infiltration into Ni/YSZ tested under steam electrolysis [19,52]. Overall, introduction of cerium nanoparticles not only improves the electrocatalytic performance for CO₂ reduction reaction, but also effectively restores and even improves the performance of cells with deactivated Ni/YSZ electrodes. This is of particular interest for solid oxide stack technologies that use compression seals, such as mica paper or Thermiculite® [50]. Unlike glass sealants, compression seals do not permanently glue the electrode/electrolyte assembly with the interconnectors or the current collector plates. Therefore degraded cells can be recovered upon disassembling from the stack and eventually infiltrated with NiCeO₂ NPs in order to restore their performance.

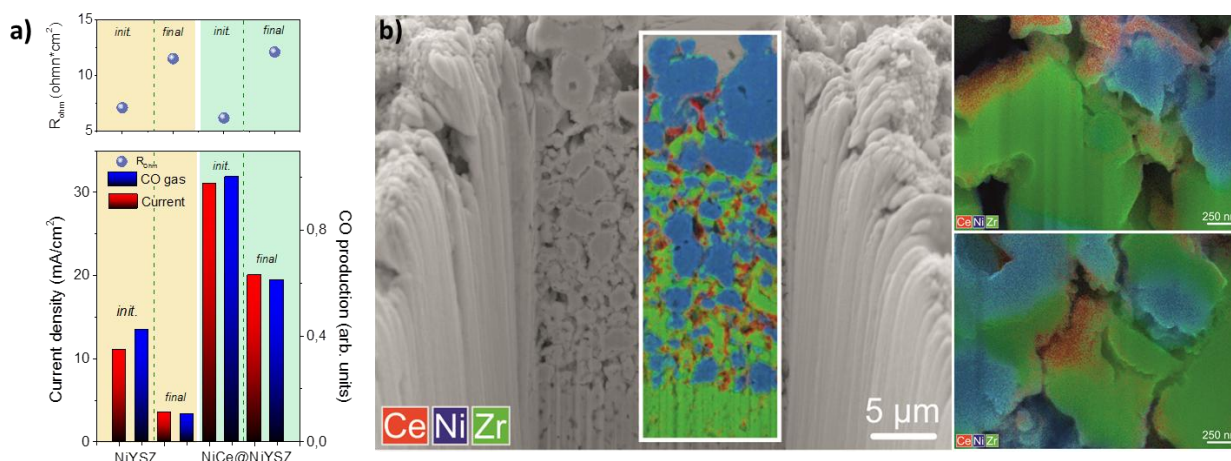


Figure 6. a) The current density and the gas phase CO production at -2.0 V (bottom) as well as the R_{ohm} at O.C. (top) of NiYSZ and NiCe@NiYSZ electrodes, before and after the redox degradation process. Reaction conditions: 1 mbar CO₂ at 550°C, **b)** FIB/SEM combined with EDX-mapping of the NiCe@NiYSZ electrode measured after reactivation, redox treatments and CO₂ electrolysis tests.

4. Conclusions

In this work we demonstrate the effect of NiCeO_x NPs in the electrochemical performance of Ni/YSZ cermet electrodes for direct CO₂ electroreduction. One-step infiltration process of NiYSZ electrodes with NiCeO_x NPs induces up to 3-times increase of the electrocatalytic performance. Morphological analysis of the cells demonstrates that NiCeO_x NPs are homogeneously distributed into the Ni/YSZ electrode volume, while quasi in situ XPS characterization reveals an enhanced reducibility of the modified cells. Finally, it is shown that impregnation with the NiCeO_x NPs can be a promising strategy to re-activate aged Ni/YSZ electrodes submitted to repeated redox cycles.

Acknowledgments

DC and JZ would like to thank the China Scholarship Council (CSC) for supporting their studies in ICPEES and FRH2 (Fédération de Recherche Hydrogène du CNRS) for the financial support. MB acknowledges financial support from Strasbourg University via the IdEX-2018 (Post-doctorants) project. Finally, DC and MB acknowledge the support of the French Agence Nationale de la Recherche (ANR), under contract No 236294 (project DuCaCO₂).

References

- [1] Posdziech O, Schwarze K, Brabandt J. Efficient hydrogen production for industry and electricity storage via high-temperature electrolysis. *Int J Hydrogen Energy* 2019;44:19089–101. <https://doi.org/10.1016/j.ijhydene.2018.05.169>.
- [2] Hauch A, Küngas R, Blennow P, Hansen AB, Hansen JB, Mathiesen B V, et al. Recent advances in solid oxide cell technology for electrolysis. *Science* (80-) 2020;370. <https://doi.org/10.1126/science.aba6118>.
- [3] Lay-Grindler E, Laurencin J, Villanova J, Cloetens P, Bleuet P, Mansuy A, et al. Degradation study by 3D reconstruction of a nickel-yttria stabilized zirconia cathode after high temperature steam electrolysis operation. *J Power Sources* 2014;269:927–36. <https://doi.org/10.1016/j.jpowsour.2014.07.066>.
- [4] Chen M, Liu Y-L, Bentzen JJ, Zhang W, Sun X, Hauch A, et al. Microstructural Degradation of Ni/YSZ Electrodes in Solid Oxide Electrolysis Cells under High Current. *J Electrochem Soc* 2013;160:F883–91. <https://doi.org/10.1149/2.098308JES>.
- [5] Ebbesen SD, Graves C, Hauch A, Jensen SH, Mogensen M. Poisoning of Solid Oxide Electrolysis Cells by Impurities. *J Electrochem Soc* 2010;157:B1419. <https://doi.org/10.1149/1.3464804>.
- [6] Ovtar S, Tong X, Bentzen JJ, Thydén KTS, Simonsen SB, Chen M. Boosting the performance and durability of Ni/YSZ cathode for hydrogen production at high current densities: Via decoration with nano-sized electrocatalysts. *Nanoscale* 2019;11:4394–406.

<https://doi.org/10.1039/c8nr07678b>.

- [7] Nechache A, Boukamp BA, Cassir M, Ringuedé A. Premature degradation study of a cathode-supported solid oxide electrolysis cell. *J Solid State Electrochem* 2018 231 2018;23:109–23. <https://doi.org/10.1007/S10008-018-4116-7>.
- [8] Tong X, Ovtar S, Brodersen K, Hendriksen PV, Chen M. Large-area solid oxide cells with La_{0.6}Sr_{0.4}CoO_{3-δ} infiltrated oxygen electrodes for electricity generation and hydrogen production. *J Power Sources* 2020;451:227742. <https://doi.org/10.1016/J.JPOWSOUR.2020.227742>.
- [9] Barnett SA, Park B-K, Scipioni R. Effect of Infiltration on Performance of Ni-YSZ Fuel Electrodes. *ECS Trans* 2019;91:1791. <https://doi.org/10.1149/09101.1791ECST>.
- [10] E. Hernández, F. Baiutti, A. Morata, M. Torrell, A. Tarancón. Infiltrated mesoporous oxygen electrodes for high temperature co-electrolysis of H₂O and CO₂ in solid oxide electrolysis cells. *J Mater Chem A* 2018;6:9699–707. <https://doi.org/10.1039/C8TA01045E>.
- [11] Park B-K, Scipioni R, Cox D, Barnett SA. Enhancement of Ni-(Y₂O₃)_{0.08}(ZrO₂)_{0.92} fuel electrode performance by infiltration of Ce_{0.8}Gd_{0.2}O_{2-δ} nanoparticles. *J Mater Chem A* 2020;8:4099–106. <https://doi.org/10.1039/C9TA12316D>.
- [12] Tong X, Hendriksen PV, Hauch A, Sun X, Chen M. An Up-scalable, Infiltration-Based Approach for Improving the Durability of Ni/YSZ Electrodes for Solid Oxide Cells. *J Electrochem Soc* 2020;167:24519. <https://doi.org/10.1149/1945-7111/ab6f5c>.
- [13] Xu J, Xue B, Liu YM, Li YX, Cao Y, Fan KN. Mesoporous Ni-doped ceria as an efficient catalyst for styrene synthesis by oxidative dehydrogenation of ethylbenzene. *Appl Catal A Gen* 2011;405:142–8. <https://doi.org/10.1016/j.apcata.2011.08.001>.
- [14] Shen M, Wang J, Shang J, An Y, Wang J, Wang W. Modification ceria-zirconia mixed oxides by doping sr using the reversed microemulsion for improved Pd-only three-way catalytic performance. *J Phys Chem C* 2009;113:1543–51. <https://doi.org/10.1021/jp808962r>.
- [15] Wang Y, Lin X, Zhang L, Xiao G, Guan C, Yang J, et al. Three-dimensional microstructural characterization of solid oxide electrolysis cell with Ce_{0.8}Gd_{0.2}O₂-infiltrated Ni/YSZ electrode using focused ion beam-scanning electron microscopy. *J Solid State Electrochem* 2021;25:1633–44. <https://doi.org/10.1007/s10008-021-04926-w>.
- [16] Gasper PJ, Lu Y, Nikiforov AY, Basu SN, Gopalan S, Pal UB. Detailed electrochemical performance and microstructural characterization of nickel – Yttria stabilized zirconia cermet anodes infiltrated with nickel, gadolinium doped ceria, and nickel – Gadolinium doped ceria nanoparticles. *J Power Sources* 2020;447:227357. <https://doi.org/10.1016/j.jpowsour.2019.227357>.
- [17] Skafte TL, Hjelm J, Blennow P, Graves C. Reactivating the Ni-YSZ electrode in solid oxide cells and stacks by infiltration. *J Power Sources* 2018;378:685–90. <https://doi.org/10.1016/j.jpowsour.2018.01.021>.
- [18] Fernández-González R, Ruiz-Morales JC, Canales-Vázquez J, Jurado JR, Makradi A, Núñez P. Decreasing the polarisation resistance of a Ni-YSZ solid oxide fuel cell anode by infiltration of a ceria-based solution. *Int J Hydrogen Energy* 2016;41:19731–6. <https://doi.org/10.1016/j.ijhydene.2016.03.092>.
- [19] Tong X, Ovtar S, Brodersen K, Hendriksen PV, Chen M. A 4 × 4 cm² Nanoengineered Solid Oxide Electrolysis Cell for Efficient and Durable Hydrogen Production. *ACS Appl Mater Interfaces* 2019;11:25996–6004. <https://doi.org/10.1021/acsami.9b07749>.
- [20] Chen Y, Bunch J, Jin C, Yang C, Chen F. Performance enhancement of Ni-YSZ electrode by

- impregnation of Mo_{0.1}Ce_{0.9}O_{2+δ}. *J Power Sources* 2012;204:40–5. <https://doi.org/10.1016/J.JPOWSOUR.2012.01.019>.
- [21] Skafte TL, Guan Z, Machala ML, Gopal CB, Monti M, Martinez L, et al. Selective high-temperature CO₂ electrolysis enabled by oxidized carbon intermediates. *Nat Energy* 2019;4:846–55. <https://doi.org/10.1038/s41560-019-0457-4>.
- [22] Chueh WC, Hao Y, Jung W, Haile SM. High electrochemical activity of the oxide phase in model ceria-Pt and ceria-Ni composite anodes. *Nat Mater* 2012;11:155–61. <https://doi.org/10.1038/nmat3184>.
- [23] Lu Y, Gasper P, Nikiforov AY, Pal UB, Gopalan S, Basu SN. Co-infiltration of Nickel and Mixed Conducting Gd_{0.1}Ce_{0.9}O_{2-δ} and La_{0.6}Sr_{0.3}Ni_{0.15}Cr_{0.85}O_{3-δ} Phases in Ni-YSZ Anodes for Improved Stability and Performance. *Jom* 2019;71:3835–47. <https://doi.org/10.1007/s11837-019-03723-1>.
- [24] Thieu CA, Yang S, Ji H II, Kim H, Yoon KJ, Lee JH, et al. Achieving performance and longevity with butane-operated low-temperature solid oxide fuel cells using low-cost Cu and CeO₂ catalysts. *J Mater Chem A* 2022;10:2460–73. <https://doi.org/10.1039/d1ta06922e>.
- [25] Wang J, Wang T, Yu L, Wei T, Hu X, Ye Z, et al. Catalytic CeO₂ washcoat over microchanneled supporting cathodes of solid oxide electrolysis cells for efficient and stable CO₂ reduction. *J Power Sources* 2019;412:344–9. <https://doi.org/10.1016/j.jpowsour.2018.11.050>.
- [26] Hong J, Balamurugan C, Im H-N, Jeon S-Y, Yoo Y-S, Song S-J. The Electrochemical Properties of Nanocrystalline Gd_{0.1} Ce_{0.9} O_{1.95} Infiltrated Solid Oxide Co-Electrolysis Cells. *J Electrochem Soc* 2018;165:F132–41. <https://doi.org/10.1149/2.0211803jes>.
- [27] Lyu Z, Wang Y, Zhang Y, Han M. Solid oxide fuel cells fueled by simulated biogas: Comparison of anode modification by infiltration and reforming catalytic layer. *Chem Eng J* 2020;393. <https://doi.org/10.1016/j.cej.2020.124755>.
- [28] Zhang Y, Fan H, Han M. Stability of Ni-YSZ Anode for SOFCs in Methane Fuel: The Effects of Infiltrating La_{0.8} Sr_{0.2} FeO_{3-δ} and Gd-Doped CeO₂ Materials. *J Electrochem Soc* 2018;165:F756–63. <https://doi.org/10.1149/2.0171810jes>.
- [29] Kim-Lohsoontorn P, Kim YM, Laosiripojana N, Bae J. Gadolinium doped ceria-impregnated nickel-yttria stabilised zirconia cathode for solid oxide electrolysis cell. *Int J Hydrogen Energy* 2011;36:9420–7. <https://doi.org/10.1016/j.ijhydene.2011.04.199>.
- [30] Chen Y, Zhang Y, Lin Y, Yang Z, Su D, Han M, et al. Direct-methane solid oxide fuel cells with hierarchically porous Ni-based anode deposited with nanocatalyst layer. *Nano Energy* 2014;10:1–9. <https://doi.org/10.1016/j.nanoen.2014.08.016>.
- [31] Sumi H, Suda E, Mori M, Weber A. Infiltration of Lanthanum Doped Ceria into Nickel-Zirconia Anodes for Direct Butane Utilization in Solid Oxide Fuel Cells. *J Electrochem Soc* 2019;166:F301–5. <https://doi.org/10.1149/2.0891904jes>.
- [32] Chen D, Barreau M, Turczyniak-Surdacka S, Sobczak K, Strawski M, Salle ALG La, et al. Ceria nanoparticles as promoters of CO₂ electroreduction on Ni/YSZ: an efficient preparation strategy and insights into the catalytic promotion mechanism. *Nano Energy* 2022;101:107564. <https://doi.org/10.1016/j.nanoen.2022.107564>.
- [33] Barreau M, Chen D, Zhang J, Papaefthimiou V, Petit C, Salusso D, et al. Synthesis of Ni-doped ceria nanoparticles and their unusual surface reduction in hydrogen. *Mater Today Chem* 2022;26:101011. <https://doi.org/10.1016/j.mtchem.2022.101011>.
- [34] Chen D, Barreau M, Dintzer T, Bournel F, Gallet J-J, Zafeiratos S. Surface oxidation of Ni-cermet electrodes by CO₂ and H₂O and how to moderate it. *J Energy Chem* 2022;67:300–8.

- <https://doi.org/10.1016/j.jechem.2021.10.002>.
- [35] Chen D, Niakolas DK, Papaefthimiou V, Ioannidou E, Neophytides SG, Zafeiratos S. How the surface state of nickel/gadolinium-doped ceria cathodes influences the electrochemical performance in direct CO₂ electrolysis. *J Catal* 2021;404:518–28. <https://doi.org/10.1016/j.jcat.2021.10.027>.
- [36] Paloukis F, Papazisi KM, Dintzer T, Papaefthimiou V, Saveleva VA, Balomenou SP, et al. Insights into the Surface Reactivity of Cermet and Perovskite Electrodes in Oxidizing, Reducing, and Humid Environments. *ACS Appl Mater Interfaces* 2017;9:25265–77. <https://doi.org/10.1021/acsami.7b05721>.
- [37] Papaefthimiou V, Niakolas DK, Paloukis F, Dintzer T, Zafeiratos S. Is Steam an Oxidant or a Reductant for Nickel/Doped-Ceria Cermets? *ChemPhysChem* 2017;18:164–70. <https://doi.org/10.1002/cphc.201600948>.
- [38] Mewafy B, Paloukis F, Papazisi KM, Balomenou SP, Luo W, Teschner D, et al. Influence of Surface State on the Electrochemical Performance of Nickel-Based Cermet Electrodes during Steam Electrolysis. *ACS Appl Energy Mater* 2019;2:7045–55. <https://doi.org/10.1021/acsaem.9b00779>.
- [39] Caliandro P, Nakajo A, Diethelm S, Van herle J. Model-assisted identification of solid oxide cell elementary processes by electrochemical impedance spectroscopy measurements. *J Power Sources* 2019;436:226838. <https://doi.org/https://doi.org/10.1016/j.jpowsour.2019.226838>.
- [40] Qi W, Gan Y, Yin D, Li Z, Wu G, Xie K, et al. Remarkable chemical adsorption of manganese-doped titanate for direct carbon dioxide electrolysis. *J Mater Chem A* 2014;2:6904–15. <https://doi.org/10.1039/c4ta00344f>.
- [41] Liu S, Liu Q, Luo JL. The excellence of La(Sr)Fe(Ni)O₃ as an active and efficient cathode for direct CO₂ electrochemical reduction at elevated temperatures. *J Mater Chem A* 2017;5:2673–80. <https://doi.org/10.1039/c6ta09151b>.
- [42] Miyawaki K, Kishimoto M, Iwai H, Saito M, Yoshida H. Comprehensive understanding of the active thickness in solid oxide fuel cell anodes using experimental, numerical and semi-analytical approach. *J Power Sources* 2014;267:503–14. <https://doi.org/10.1016/j.jpowsour.2014.05.112>.
- [43] Sumi H, Yamaguchi T, Shimada H, Hamamoto K, Suzuki T, Barnett SA. Direct Butane Utilization on Ni-(Y₂O₃)_{0.08}(ZrO₂)_{0.92}-(Ce_{0.9}Gd_{0.1})O_{1.95} Composite Anode-Supported Microtubular Solid Oxide Fuel Cells. *Electrocatalysis* 2017;8:288–93. <https://doi.org/10.1007/s12678-017-0369-7>.
- [44] Song Y, Zhou Z, Zhang X, Zhou Y, Gong H, Lv H, et al. Pure CO₂ electrolysis over an Ni/YSZ cathode in a solid oxide electrolysis cell. *J Mater Chem A* 2018;6:13661–7. <https://doi.org/10.1039/c8ta02858c>.
- [45] Tan Z, Song JT, Takagaki A, Ishihara T. Infiltration of cerium into a NiO–YSZ tubular substrate for solid oxide reversible cells using a LSGM electrolyte film. *J Mater Chem A* 2021;9:1530–40. <https://doi.org/10.1039/D0TA08564B>.
- [46] Papaefthimiou V, Niakolas DKDK, Paloukis F, Teschner D, Knop-Gericke A, Haevecker M, et al. Operando observation of nickel/ceria electrode surfaces during intermediate temperature steam electrolysis. *J Catal* 2017;352:305–13. <https://doi.org/10.1016/j.jcat.2017.06.005>.
- [47] Law YT, Skála T, Píš I, Nehasil V, Vondráček M, Zafeiratos S. Bimetallic nickel-cobalt nanosized layers supported on polar ZnO surfaces: Metal-support interaction and alloy effects studied by synchrotron radiation X-ray photoelectron spectroscopy. *J Phys Chem C* 2012;116. <https://doi.org/10.1021/jp301219u>.

- [48] Papaefthimiou V, Shishkin M, Niakolas DK, Athanasiou M, Law YT, Arrigo R, et al. On the active surface state of nickel-ceria solid oxide fuel cell anodes during methane electrooxidation. *Adv Energy Mater* 2013;3:762–9. <https://doi.org/10.1002/aenm.201200727>.
- [49] Sala EM, Mazzanti N, Mogensen MB, Chatzichristodoulou C. Current understanding of ceria surfaces for CO₂ reduction in SOECs and future prospects – A review. *Solid State Ionics* 2022;375:115833. <https://doi.org/https://doi.org/10.1016/j.ssi.2021.115833>.
- [50] Zheng Y, Wang J, Yu B, Zhang W, Chen J, Qiao J, et al. A review of high temperature co-electrolysis of H₂O and CO₂ to produce sustainable fuels using solid oxide electrolysis cells (SOECs): Advanced materials and technology. *Chem Soc Rev* 2017;46:1427–63. <https://doi.org/10.1039/c6cs00403b>.
- [51] Tan J, Lee D, Ahn J, Kim B, Kim J, Moon J. Thermally driven in situ exsolution of Ni nanoparticles from (Ni_x)GdCeO₂ for high-performance solid oxide fuel cells. *J Mater Chem A* 2018;6:18133–42. <https://doi.org/10.1039/C8TA05978K>.
- [52] Torknik FS, Keyanpour-Rad M, Maghsoudipour A, Choi GM. Effect of microstructure refinement on performance of Ni/Ce_{0.8}Gd_{0.2}O_{1.9} anodes for low temperature solid oxide fuel cell. *Ceram Int* 2014;40:1341–50. <https://doi.org/https://doi.org/10.1016/j.ceramint.2013.07.015>.